IECON 2025 – 51st Annual Conference of the IEEE Industrial Electronics Society | 979-8-3315-9681-1/25/$31.00 ©2025 IEEE | DOI: 10.1109/IECON58223.2025.11221537

Modeling of the Inverter Current Distortion in the Double-sided LCC Compensation for Inductive Power Transfer Systems

F. Grazian[1], G. Yu[2], C. Riekerk[2], W. Shi[2], J. Dong[2], G. Zhu[3], Thiago B. Soeiro[4], and P. Bauer[2]

[1]Department of Electrical Engineering, Eindhoven University of Technology, Eindhoven, The Netherlands.
[2]Department of Electrical Sustainable Energy, Delft University of Technology, Delft, The Netherlands.
[3]Department of Electrical and Electronic Engineering, City University of Hong Kong, Kowloon Tong, Honk Kong.
[4]Department of Electrical Engineering, University of Twente, Enschede, The Netherlands.

***Abstract*—The double-sided LCC (DLCC) compensation has been widely used in inductive power transfer (IPT) systems because it has a load-independent current source output directly proportional to the coils' coupling, which makes it inherently safe against misalignment. The input current of the DLCC typically has high harmonic distortion due to the low-pass filter characteristic of the input LC components. Consequently, predicting the inverter's turn-off current through circuit modeling using the first-harmonic approximation (FHA) would result in a significant estimation error. However, an accurate computation is essential to determine whether the inverter's zero-voltage switching (ZVS) turn-on is achieved. This paper defines an analytical model that effectively predicts the inverter turn-off current point for any operating condition, i.e., when the diode rectifier operates in continuous and discontinuous conduction modes. It has been found that the inverter turn-off current depends on the loading condition. Therefore, the proposed method is based on modeling the equivalent load as the rectifier together with the battery. Experimental verification has been conducted using two IPT systems with nominal power levels of 3.7 kW and 7.7 kW.**

***Index Terms*—Compensation networks, electric vehicles, inductive power transfer, wireless charging.**

I. Introduction

Inductive power transfer (IPT) employed for wireless battery charging has been gaining interest in the electric vehicle (EV) industry, mainly because it would solve the inconvenience of drivers handling charging cables.

The core of IPT systems consists of coupled coils that form a loosely coupled transformer (LCT) since a relatively large air gap separates them. These coupled coils exchange electrical energy through a high-frequency magnetic field whose operating frequency is constrained between $79\,\mathrm{kHz}$ and $90\,\mathrm{kHz}$ in light-duty EV applications [1]. The LCT has a relatively low coupling factor, e.g., $k < 0.4$, meaning that the leakage inductance of both the primary and secondary circuits would be considerably high. Passive components are used to compensate for that inductance to minimize the circulating reactive power. These circuit elements are normally called compensation networks. The one-component compensation networks consist of a capacitor that can be connected in series or parallel to the coil. Among the four possible combinations, the series-series (S-S) compensation is the most commonly used in EV charging, as its parameters can be tuned independently of the coils' alignment and loading conditions, and exhibits a load-independent output current source behavior [2]. Nevertheless, the transferred output power is inversely proportional to k, which makes the IPT system not intrinsically safe against misalignment.

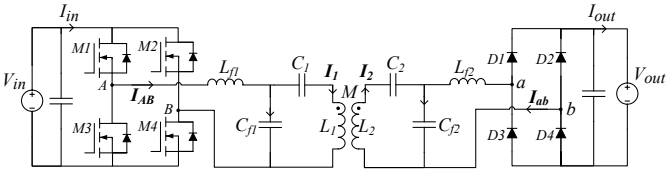

Fig. 1. Equivalent circuit of an IPT system with the DLCC compensation.

Additionally, multi-component compensation networks have been used in IPT systems, of which the LC and LCC circuits are common examples. Both employ compensation inductors and capacitors that are tuned based on the T-type resonant circuit. The LCC employs one more capacitor connected in series to the coupled coil, allowing smaller compensation inductors to be selected. The LCC compensation can be used only at the primary or the secondary circuit, as demonstrated in [3], which proposes an LCC-S compensation with more robust power transfer over the misalignment than the LC compensation. On the other hand, the compensation network takes the name of double-sided LCC (DLCC) when the LCC is used for both circuits, which typical configuration is shown in Fig. 1. Thereby, L_{f1} and L_{f2} depict the compensation inductors, C_{f1} and C_{f2} symbolize the parallel compensation capacitors, C_1 and C_2 stand for the series compensation capacitors, and L_1 and L_2 describe the self-inductance of the coupled coils. The great advantage of the DLCC compensation is that the delivered output power can be selected by choosing the compensation inductances without the need to modify the LCT. In contrast to the S-S compensation, the output power is directly proportional to k, making the DLCC especially suitable for applications with large misalignment tolerances, e.g., in dynamic wireless charging. Moreover, [4] proved that IPT systems employing the DLCC are less sensitive to the parameters' mistuning than those with the S-S compensation.

The DLCC compensation has been widely analyzed in the literature [4]–[9]. A well-known paper on the DLCC compensation for IPT systems is [5], which defines the parameter tuning method and analyzes the circuit through the

first-harmonic approximation (FHA). In IPT systems, it is crucial to accurately predict the inverter's turn-off current to determine whether zero-voltage switching (ZVS) turn-on can be achieved. However, [5] has acknowledged that the inverter's current can be heavily distorted due to the low-pass filter characteristic of the input LC circuit consisting of L_{f1} and C_{f1}. Because of those high-order harmonic components, the analytical prediction of the turn-off current would not be accurate simply by using the FHA analysis. Therefore, the inverter's current is assessed by considering the high-order harmonic components, and based on those, the inverter's turn-off current has been estimated. As a result, this analytical estimation of the turn-off current is relatively accurate when the diode rectifier operates in continuous conduction mode (CCM). However, significant errors are still found in discontinuous conduction mode (DCM). Using a similar approach, [6] and [7] have defined guidelines for selecting C_2 to achieve the inverter turn-off current, thereby guaranteeing ZVS turn-on operation. Nevertheless, detailed modeling of the turn-off current is not provided. Likewise, the same modeling gap is present in [4] and [8]. All in all, no analytical model has been proposed yet that can accurately predict the current flowing through L_{f1} for any loading condition.

As the main contribution, this paper proposes an analytical method to predict the distortion of the H-bridge inverter's current when the diode rectifier is operating in both CCM and DCM. This method is beneficial for assessing whether the inverter can achieve ZVS turn-on in any operating condition without performing circuit simulations.

II. Modeling of the DLCC compensation

The parameters turning of the DLCC compensation network illustrated in Fig. 1 generally follows the approach used in [5]. This is summarized in (2), where $\omega_0 = 2\pi f_0$ is the angular resonant frequency. As a result of (2), at both sides of the primary and the secondary circuits, the compensation inductor resonates with the parallel capacitor at the same ω_0 as the coupled coil together with the series compensation capacitor.

Moreover, the mutual inductance M between the coupled coils is defined in (3) depending on the coupling factor k.

$$L_{fi}C_{fi} = \frac{1}{\omega_0^2}, \quad L_i - L_{fi} = \frac{1}{\omega_0^2 C_i} \qquad i = 1, 2 \tag{2}$$

$$M = k\sqrt{L_1 L_2} \tag{3}$$

A. Phasor convention based on the FHA

The equivalent circuit of an IPT system using the DLCC compensation is shown in Fig. 2, including the components' equivalent series resistance. The operating points of the circuit in Fig. 2 can be computed in terms of voltages and currents through the Kirchhoff voltage law in (1) with the circuit impedances defined in (4)-(6).

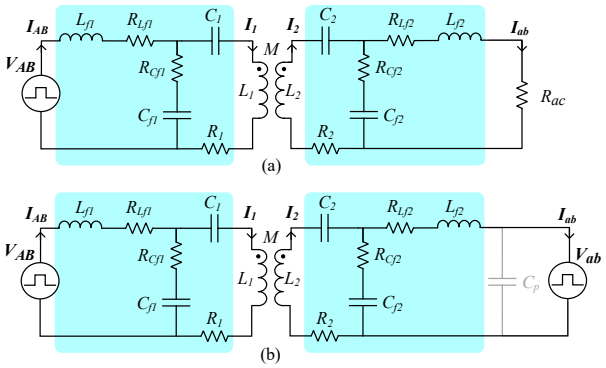

Fig. 2. Equivalent circuit of 1 where the load is modeled as: (a) the equivalent resistance R_{ac} in (8); (b) the voltage source $\boldsymbol{V_{ab}}$ in (9).

$$\boldsymbol{Z_{L_{f_1}}} = R_{L_{f1}} + j\omega L_{f1}, \quad \boldsymbol{Z_{C_{f_1}}} = R_{C_{f1}} + \frac{1}{j\omega C_{f1}} \tag{4}$$

$$\boldsymbol{Z_{L_{f_2}}} = R_{L_{f2}} + j\omega L_{f2}, \quad \boldsymbol{Z_{C_{f_2}}} = R_{C_{f2}} + \frac{1}{j\omega C_{f2}} \tag{5}$$

$$\boldsymbol{Z_1} = R_1 + j\omega L_1 + \frac{1}{j\omega C_1}, \quad \boldsymbol{Z_2} = R_2 + j\omega L_2 + \frac{1}{j\omega C_2} \tag{6}$$

The input voltage source $\boldsymbol{V_{AB}}$ defined in (7) is used according to the FHA [10]. $\boldsymbol{V_{AB}}$ uses the phasor convention, and it is specified in terms of its absolute value and phase angle. $\boldsymbol{V_{AB}}$ is taken as the reference, i.e., $\phi_{V_{AB}}$. The circuit in Fig. 2(a) models the load as the equivalent resistance R_{ac} in (8), as explained in [10]. In this case, $\boldsymbol{V_{ab}}$ in (1) should be replaced with $\boldsymbol{V_{ab}}$=$R_{ac}\boldsymbol{I_{ab}}$. Alternatively, the circuit in Fig. 2(b) models the load as the voltage source $\boldsymbol{V_{ab}}$ defined in (9). This representation is closer to reality if the load battery is directly connected to the rectifier circuit, as shown in Fig. 1.

$$\boldsymbol{V_{AB}} = V_{AB}\underline{/0} = \frac{4}{\pi}V_{in} \tag{7}$$

$$R_{ac} = \frac{8}{\pi^2}R_L = \frac{8}{\pi^2}\frac{V_{out}}{I_{out}} = \frac{V_{ab}}{I_{ab}} \tag{8}$$

$$\boldsymbol{V_{ab}} = V_{ab}\underline{/\phi_{V_{ab}}} = \frac{4}{\pi}V_{out}\underline{/\phi_{V_{ab}}} \tag{9}$$

Moreover, another useful circuit parameter is the input impedance $\boldsymbol{Z_{in}} = \boldsymbol{V_{AB}}/\boldsymbol{I_{AB}}$ defined in (10), describing the equivalent impedance of the IPT system seen from the input source $\boldsymbol{V_{AB}}$. Similarly to the approach used in [11], $\boldsymbol{Z_{in}}$ is computed through the reflected impedance $\boldsymbol{Z_r}$ in (11).

$$\boldsymbol{Z_{in}} = \boldsymbol{Z_{L_{f_1}}} + \frac{\boldsymbol{Z_{C_{f_1}}}(\boldsymbol{Z_1} + \boldsymbol{Z_r})}{\boldsymbol{Z_{C_{f_1}}} + \boldsymbol{Z_1} + \boldsymbol{Z_r}} \tag{10}$$

$$\boldsymbol{Z_r} = \frac{\omega^2 M^2}{\boldsymbol{Z_2} + \frac{(\frac{\boldsymbol{V_{ab}}}{\boldsymbol{I_{ab}}} + \boldsymbol{Z_{L_{f_2}}})\boldsymbol{Z_{C_{f_2}}}}{\frac{\boldsymbol{V_{ab}}}{\boldsymbol{I_{ab}}} + \boldsymbol{Z_{L_{f_2}}} + \boldsymbol{Z_{C_{f_2}}}}} \tag{11}$$

$$\begin{bmatrix} \boldsymbol{V_{AB}} \\ 0 \\ 0 \\ \boldsymbol{V_{ab}} \end{bmatrix} = \begin{bmatrix} \boldsymbol{Z_{L_{f_1}}} + \boldsymbol{Z_{C_{f_1}}} & -\boldsymbol{Z_{C_{f_1}}} & 0 & 0 \\ -\boldsymbol{Z_{C_{f_1}}} & \boldsymbol{Z_1} + \boldsymbol{Z_{C_{f_1}}} & j\omega M & 0 \\ 0 & j\omega M & \boldsymbol{Z_2} + \boldsymbol{Z_{C_{f_2}}} & -\boldsymbol{Z_{C_{f_2}}} \\ 0 & 0 & \boldsymbol{Z_{C_{f_2}}} & -\boldsymbol{Z_{L_{f_2}}} - \boldsymbol{Z_{C_{f_2}}} \end{bmatrix} \begin{bmatrix} \boldsymbol{I_{AB}} \\ \boldsymbol{I_1} \\ \boldsymbol{I_2} \\ \boldsymbol{I_{ab}} \end{bmatrix} \tag{1}$$

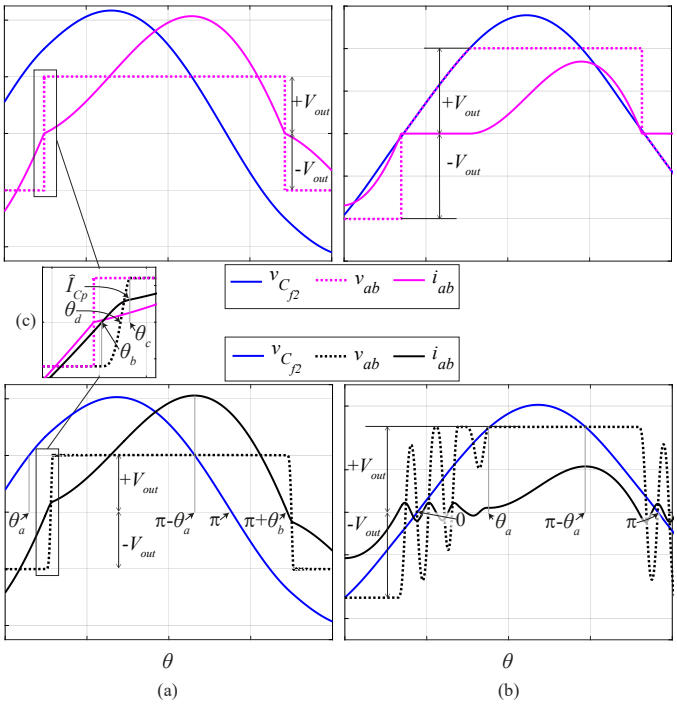

Fig. 3. Typical conduction of the diode rectifier depending on the voltage across C_{f2}: (a) CCM, (b) DCM. The top plots result from circuit simulations using ideal diode models, while the bottom plots result from circuit simulations using the physical diode characteristics. (c) Zoom-in of the turn-on transition of the diodes D1 and D4 in Fig. 1. It must be noted that the phase angle of $v_{C_{f2}}$ is considered as the reference, i.e., $\phi_{V_{Cf2}}$=0, and θ is considered as the x-axis such that θ=$\omega_0 \cdot t$.

B. Equivalent load of the rectifier and the battery

Fig. 1 shows the circuit schematic of an IPT system with DLCC compensation, in which the load consists of a full-wave diode rectifier connected to an output voltage source representing the battery load. As illustrated in Fig. 2, the modeling of the equivalent load typically considers either the resistance R_{ac} defined in (8) or the voltage source $\boldsymbol{V_{ab}}$ defined in (9). Efforts to model the equivalent load in the DLCC analytically have been made in [12] and [13]. However, both consider the major assumption that the diode rectifier always operates in CCM. Moreover, [12] defines a model valid for a resistive load type, while [5] and [13] consider the load based on the voltage source model with a fix phase angle, i.e., $\phi_{V_{ab}}$=$-\frac{\pi}{2}$. These load modeling strategies might result in large errors due to the two following factors.

The first factor is the conduction mode of the diode rectifier, which typical operating waveforms are shown in Fig. 3. The top plots result from a rectifier using the ideal diode model, while the bottom ones result from a rectifier considering the on-state characteristics of the diode. For instance, the current i_{ab} would flow through L_{f2} only when $v_{Cf2} > v_{ab}$. If this condition is always satisfied during the switching cycle, the diode rectifier will operate in CCM, which examples are illustrated in Fig. 3(a). On the other hand, if $v_{Cf2} > v_{ab}$ is not always satisfied for the entire switching cycle, the diode rectifier will likely operate in DCM, which examples are illustrated in Fig. 3(b). Especially in DCM, the load characteristic fundamentally differs from the case of the equivalent resistive load. Additionally, the phase angle of the load voltage v_{ab} would also differ depending on the rectifier's conduction.

TABLE I
DEFINITION OF THE ANGLES USED IN FIG. 3 WHERE $\phi_{V_{Cf2}}$ IS CONSIDERED AS A REFERENCE.

Parameter	Definition
θ_a	$v_{Cf2}(\theta_a) = +V_{out}$
θ_b	$v_{ab}(\theta_b) = -V_{out}$
θ_c	$v_{ab}(\theta_c) = V_{out}$
θ_d	$v_{ab}(\theta_d) = 0$

The second factor is the parasitic capacitance of the diode rectifier, which lumped equivalent value can be modeled as the capacitor C_p shown in Fig. 2(b), connected in parallel to the output voltage source $\boldsymbol{V_{ab}}$. This capacitance must be discharged and charged as $\boldsymbol{V_{ab}}$ inverts polarity. From the zoom in Fig. 3(c), this capacitive behavior results in a delay of v_{ab} with respect to the case of an ideal diode rectifier. This results in v_{ab} and i_{ab} being out of phase as shown in Fig. 3(c). All angles in Fig. 3 are listed and defined in Table I. When analyzing the rectifier's conduction, $\phi_{V_{Cf2}}$ is considered as a reference, i.e., $\phi_{V_{Cf2}}$=0.

The peak current $\hat{I}_{Cp}$ in Fig. 3(c) is defined as $\hat{I}_{Cp}$=$i_{ab}(\theta_c)$, which can be found by analyzing $i_{ab}(\theta)$ which, around its zero crossing, can be approximated as

$$i_{ab}(\theta) = I_{ab}\sin(\theta - \theta_b) \tag{12}$$

where, according to the FHA [10], the absolute value I_{ab} is defined as I_{ab}=$\frac{\pi}{2}I_{out}$ and I_{out} is the DC output current defined by the battery charging cycle.

In the interval $[\theta_b; \theta_c]$, $v_{ab}(\theta)$ can be written as (13). Specifically, for θ=θ_c, (14) can be found which results in (15). Finally, from (15), $\hat{I}_{Cp}$=$I_{ab}\sin(\theta_c - \theta_b)$ can be computed.

$$v_{ab}(\theta) = -V_{out} + \frac{1}{\omega_0 C_p}\int_{\theta_b}^{\theta} I_{ab}\sin(\theta - \theta_b)\,d\theta \tag{13}$$

$$2 \cdot V_{out} = \frac{1}{\omega_0 C_p}\int_{\theta_b}^{\theta_c} I_{ab}\sin(\theta - \theta_b)\,d\theta \tag{14}$$

$$\theta_{C_p} = \theta_c - \theta_b = \cos^{-1}\left(1 - \frac{2V_{out}\omega_0 C_p}{I_{ab}}\right) \tag{15}$$

III. MODELING OF THE INVERTER CURRENT DISTORTION

The distortion of i_{AB} must be known to assess whether the H-bridge inverter realizes the desired ZVS turn-on operation. This can be computed by considering the higher-order harmonics introduced by the input and output square wave voltage sources shown in Fig. 2, meaning that the circuit modeling in Section II-A must be extended.

A. Condition for the H-bridge's ZVS turn-on operation

As explained in [5] and [14], the ZVS turn-on is realized when the output current i_{AB} from the H-bridge inverter in Fig. 1 lags the inverted voltage v_{AB}. This means that the H-bridge inverter must operate in the inductive region of the resonant circuit. For that purpose, all MOSFETs must be switched off before the current crosses zero. During the dead time t_{dead}, the remaining current would flow through the anti-parallel

diodes of the MOSFETs that were blocking the input voltage V_{in}. This turn-off current level has to be large enough to discharge the equivalent drain-source capacitance C_{ds} of those MOSFETs before they are turned on and start conducting. Additionally, during t_{dead}, the C_{ds} of the MOSFETs that were just switched off must be charged to block V_{in}.

The minimum turn-off current $I_{OFF,min}$ that ensures the ZVS turn-on can be calculated as shown in (16). In (16), it is assumed that the turn-off current I_{OFF} is constant. However, due to the resonant characteristic, I_{OFF} likely has a sinusoidal shape. This means that I_{OFF} should be larger than $I_{OFF,min}$ to guarantee the ZVS turn-on operation of the inverter. The safety margin s_m, such that $s_m > 1$, must be defined and calibrated during the commissioning phase depending on C_{ds} of the selected MOSFETs. At the same time, setting the operation too deep into the inductive region is not preferable because this would increase the turn-off losses and eventually worsen the power transfer efficiency due to a higher circulating reactive current. Therefore, the turn-off current I_{OFF} must be tuned to be equal or slightly larger than $s_m \cdot I_{OFF,min}$.

$$I_{OFF,min} \approx \frac{2 \cdot C_{ds} \cdot V_{in,max}}{t_{dead}} \tag{16}$$

B. Analysis of the harmonic components of i_{AB}

From the Fourier series of a square wave, the input and output voltage sources in Fig. 2(b) can be expressed in the time domain as

$$v_{AB}(t) = \sum_{n=1,3,5...}^{\infty} \frac{4}{\pi}\frac{1}{n} V_{in} \cdot \sin(n\omega_0 t) \tag{17}$$

$$v_{ab}(t) = \sum_{n=1,3,5...}^{\infty} \frac{4}{\pi}\frac{1}{n} V_{out} \cdot \sin(n\omega_0 t + \phi_{V_{ab}}) \tag{18}$$

where the amplitude and phase angle are chosen according to the fundamental frequency component in (7) and (9). Furthermore, the Fourier series of i_{AB} can be written as

$$i_{AB}(t) = \sum_{n=1,3,5...}^{\infty} I_{AB,n} \cdot \sin(n\omega_0 t + \phi_{I_{AB,n}}) \tag{19}$$

where $I_{AB,n}$ and $\phi_{I_{AB,n}}$ are respectively the current amplitude and phase angle of the n-th harmonic component. These can be calculated through the circuit analysis in the frequency domain defined in Section II-A by imposing $\omega{=}n{\cdot}\omega_0$. This means that $I_{AB,n}$ and $\phi_{I_{AB,n}}$ can be computed as depicted in (20).

$$\boldsymbol{I_{AB,n}} = I_{AB,n}\underline{/\phi_{I_{AB,n}}} = \frac{\boldsymbol{V_{AB,n}}}{\boldsymbol{Z_{in,n}}} = \frac{\frac{4}{\pi}\frac{1}{n}V_{in}}{Z_{in,n}\underline{/\phi_{Z_{in,n}}}} \tag{20}$$

After that, the turn-off current I_{OFF} of the H-bridge inverter can be computed from (19) considering $t{=}\frac{T_0}{2}$. This results in

$$I_{OFF} = i_{AB}(\tfrac{T_0}{2}) = \sum_{n=1,3,5...}^{\infty} I_{AB,n} \cdot \sin(n\pi + \phi_{I_{AB,n}}) \tag{21}$$

The computation of $\boldsymbol{I_{AB,n}}$ depends on the input impedance $\boldsymbol{Z_{in,n}}$, which, according to (11) and (10), depends on the loading condition. The equivalent load can be modeled as the equivalent resistance $R_{ac,n}$, which circuit is shown in Fig. 2(a). Alternatively, it can be modeled as the output voltage source $\boldsymbol{V_{ab,n}}$, as shown in Fig. 2(b).

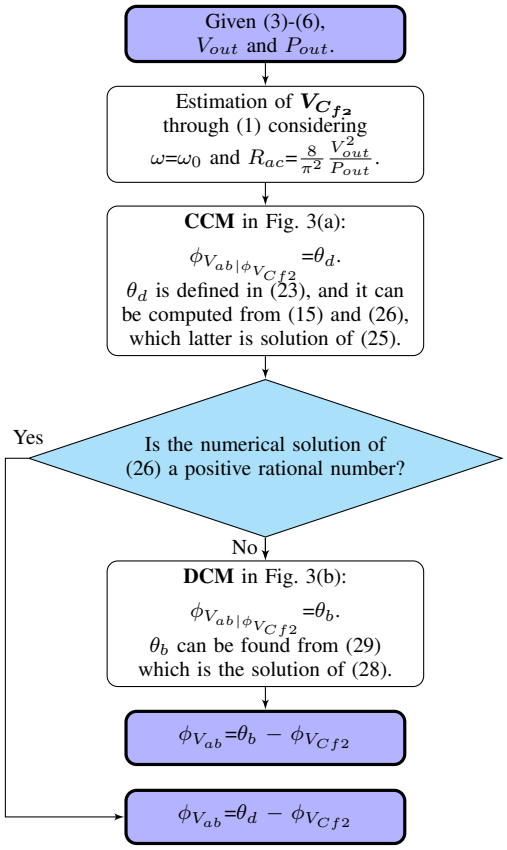

Fig. 4. Flowchart of the proposed computation method for $\phi_{V_{ab}}$. First, the process assumes that the diode rectifier operates in CCM. If that solution is invalid, the rectifier operates in DCM, and the relative solution is found.

It is interesting to assess whether the two equivalent load models in Fig. 2 result in the same estimation of $i_{AB}(t)$. From (18), it can be found that $\boldsymbol{V_{ab,n}}{=}\frac{4}{\pi}\frac{1}{n}V_{out}\underline{/\phi_{V_{ab}}}$. Therefore, the comparison between $i_{AB}(t)$ resulting from modeling the load as $R_{ac,n}$ or $\boldsymbol{V_{ab,n}}$ can be done only if $\phi_{V_{ab}}$ is known. Based on the analysis of the fundamental frequency components, the output voltage source $\boldsymbol{V_{ab}}$ leads to $\boldsymbol{V_{AB}}$ of $\pi/2$, which means that $\boldsymbol{V_{ab,n}} {=}\frac{4}{\pi}\frac{1}{n}V_{out}\underline{/-\pi/2}$. However, Fig. 3 shows that this might be an improper assumption since $\phi_{V_{ab}}$ also depends on the rectifier conduction. Therefore, for accurate analysis, $\phi_{V_{ab}}$ must be computed based on the operation.

C. Proposed computation method for $\phi_{V_{ab}}$

Fig. 3 shows that the voltage across C_{f2} and the amplitude of v_{ab}, i.e., V_{out}, influence the conduction of the diode rectifier and, consequently, v_{ab} and i_{ab}. In this analysis, it is considered that V_{out} is set by the battery, and the output power P_{out} is set by the battery charging cycle. To compute $\phi_{V_{ab}}$ at the chosen operating conditions, it is essential to find $v_{C_{f2}}$. This process is summarized in the flowchart of Fig. 4.

1) Computation of $v_{C_{f2}}$ from the FHA: As a first step approximation, the amplitude and phase angle of $V_{C_{f2}}$ can be found from the circuit analysis of Section II-A performed

using the FHA, i.e., at ω=ω_0. Since V_{out} and P_{out} are given, hereby the load is modelled as R_{ac}=$\frac{8}{\pi^2}\frac{V_{out}^2}{P_{out}}$. According to Fig. 3, $v_{C_{f2}}$ is taken as the reference in the analysis of the rectifier conduction, meaning that the phase angle $\phi_{V_{Cf2}}$=0. Therefore, considering that θ=$\omega_0 \cdot t$, $v_{C_{f2}}$ results in

$$v_{C_{f2}}(\theta) = V_{C_{f2}} \sin\theta \tag{22}$$

First, the computation of $\phi_{V_{ab}}$ is performed considering the CCM of the diode rectifier. If the solution is not a positive rational number, the diode rectifier operates in DCM and the computation of $\phi_{V_{ab}}$ is performed for that case.

2) CCM: According to Fig. 3(a), the phase angle of v_{ab} with respect to $\phi_{V_{C_{f2}}}$ is $\phi_{V_{ab}}$=θ_d, where θ_d satisfies (13) such that $v_{ab}(\theta_d)$=0. This results in

$$\theta_d = \theta_b + \cos^{-1}\left(1 - \frac{\omega_0 C_p V_{out}}{I_{ab}}\right) \tag{23}$$

The unknown θ_b can be found by solving (25), which consists of integrating (24) in the intervals $[\theta_b;\, \theta_c]$ and $[\theta_c;\, \theta_b+\pi]$ of Fig. 3(a). In the interval $[\theta_b;\, \theta_c]$, $v_{ab}(\theta)$ is defined in (13).

$$i_{ab}(\theta) = \frac{1}{\omega_0 L_{f2}} \int [v_{C_{f2}}(\theta) - v_{ab}(\theta)]\, d\theta \tag{24}$$

$$\begin{cases} \hat{I}_{Cp} = \dfrac{1}{\omega_0 L_{f2}} \int_{\theta_b}^{\theta_c} [V_{C_{f2}} \sin(\theta) - v_{ab}(\theta)]\, d\theta \\ 0 = \hat{I}_{Cp} + \dfrac{1}{\omega_0 L_{f2}} \int_{\theta_c}^{\theta_b+\pi} [V_{C_{f2}} \sin(\theta) - V_{out}]\, d\theta \end{cases} \tag{25}$$

The system of equations in (25) is nonlinear and, to simplify its computation, θ_{C_p} is considered to be known as defined in (15). The solution of (25) is shown in (26). If the diode rectifier operates in CCM as shown in Fig. 3(a), (26) will have a rational numerical solution. Conversely, if i_{ab} decreases from $\hat{I}_{Cp}$ to zero while $v_{Cf2} < v_{ab}$, (26) will not output a valid solution meaning that the diode rectifier operates in DCM as shown in Fig. 3(b).

$$\theta_c = \cos^{-1}\left[\frac{\pi V_{out} - 2\omega_0 L_{f2}\hat{I}_{Cp} + \frac{\hat{I}_{Cp} - \theta_{C_p} I_{ab}}{\omega_0 C_p}}{2V_{C_{f2}}}\right] \tag{26}$$

Assuming that the rectifier operates in CCM, θ_b can be computed as θ_b=θ_c − θ_{C_p}, which θ_{C_p} and θ_c result from (15) and (26), respectively. At this point, θ_d can be computed according to (23). Finally, considering the convention in (1) where the input voltage source $\boldsymbol{V_{AB}}$ is the reference, the phase angle of V_{ab} results in

$$\phi_{V_{ab}} = \theta_d - \phi_{V_{Cf2}} \tag{27}$$

3) DCM: If the diode rectifier operates in DCM, i_{ab} would be approximately zero as long as $v_{Cf2} < v_{ab}$, which typical examples are shown in Fig. 3(b). In this case, (26) would not result in a rational numerical solution. According to Fig. 3(b), the phase angle of v_{ab} with respect to $\phi_{V_{C_{f2}}}$ can be approximated as $\phi_{V_{ab}}$=θ_b.

The unknown θ_b can be found by solving (28), which consists of integrating (24) over the interval $[\theta_a;\, \theta_b + \pi]$ according to Fig. 3(b).

$$\begin{cases} \theta_a = \sin^{-1}\left(\dfrac{V_{C_{f2}}}{V_{out}}\right) \\ 0 = \dfrac{1}{\omega_0 L_{f2}} \int_{\theta_a}^{\theta_b+\pi} [V_{C_{f2}} \sin(\theta) - V_{out}]\, d\theta \end{cases} \tag{28}$$

Thereby, θ_a is the phase angle corresponding to $v_{C_{f2}}(\theta_a)$=V_{out}. The solution of (28) is

$$V_{C_{f2}} \cos\theta_b - V_{out}\theta_b = V_{out}(\pi - \theta_a) - V_{C_{f2}} \cos\theta_a \tag{29}$$

Since (29) is nonlinear, the numerical solution for θ_b can be found through a parametric sweep.

Finally, considering the convention in (1) where input voltage source $\boldsymbol{V_{AB}}$ is the reference $\phi_{V_{ab}} = \theta_b - \phi_{V_{Cf2}}$.

IV. Experimental Verification

This section verifies the analytical model proposed in Section III to compute i_{AB} in (19), which includes its harmonic components and the inverter turn-off current I_{OFF} in (21).

A. Laboratory prototypes

Two laboratory prototypes have been used for the experimental verification of the proposed model, shown in Fig. 5. The values of their circuit parameters are listed in Table II. Two distinct IPT systems are considered to prove that the proposed model is valid for not only a specific circuit.

The IPT system in Fig. 5(a) is rated for 3.7 kW while the one in Fig. 5(b) is rated for 7.7 kW, corresponding to the WPT1 and WPT2 power classes defined by SAE J2954

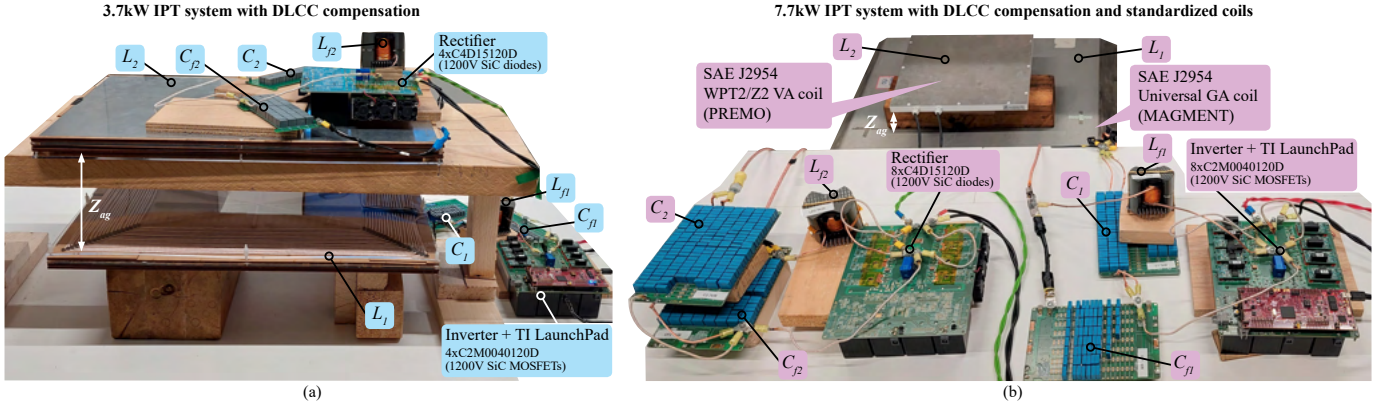

(a) (b)

Fig. 5. Laboratory demonstrators used to verify the proposed model. IPT system with DLCC compensation rated for: (a) 3.7 kW, and (b) 7.7 kW.

[15]. The two IPT systems use the same circuit board for the high-frequency inverter and rectifier. Nevertheless, the number of semiconductor devices employed doubles in the 7.7 kW IPT system in the form of hard-paralleled devices to maintain similar power losses. The operating frequency utilized in both configurations is 85 kHz. The coupled coils of the 3.7 kW

TABLE II
CIRCUIT PARAMETERS OF THE TWO LABORATORY DEMONSTRATORS IN FIG. 5, ALL MEASURED AT 85 kHz.

	3.7kW laboratory demonstrator				**7.7kW laboratory demonstrator**			
	Coupled coils				**Coupled coils**			
	M=M_{max}	M=M_{mid}	M=M_{min}		M=M_{max}	M=M_{mid}	M=M_{min}	
	M=96.35 µH Z_{ag}=10.6 cm	M=68.25 µH Z_{ag}=13.8 cm	M=50.50 µH Z_{ag}=17.0 cm	ESR (mΩ)	M=10.50 µH Z_{ag}=8.1 cm	M=8.25 µH Z_{ag}=10.2 cm	M=6.0 µH Z_{ag}=12.3 cm	ESR (mΩ)
L_1 (µH)	337.4	331.5	328.1	650	62.8	63.6	64.2	500
L_2 (µH)	223.9	218.0	215.3	440	46.4	45.8	45.5	90
	Compensation Network				**Compensation Network**			
	L_{f1} (µH) 101.1 ESR (mΩ) 45		L_{f2} (µH) 83.8 ESR (mΩ) 45		L_{f1} (µH) 30.6 ESR (mΩ) 45		L_{f2} (µH) 14.8 ESR (mΩ) 45	
	C_1 (nF) 14.4 ESR (mΩ) 55		C_2 (nF) 27.7 ESR (mΩ) 31		C_1 (nF) 110.5 ESR (mΩ) 6		C_2 (nF) 110.3 ESR (mΩ) 6	
	C_{f1} (nF) 36.0 ESR (mΩ) 25		C_{f2} (nF) 41.7 ESR (mΩ) 23		C_{f1} (nF) 113.0 ESR (mΩ) 6		C_{f2} (nF) 236.7 ESR (mΩ) 3	
	C_p=8 · 657.5 · $V_{out}^{-0.458}$ pF (see Fig. 2(b))				C_p=16 · 657.5 · $V_{out}^{-0.458}$ pF (see Fig. 2(b))			
	Compensation inductors' core PM/74/59, ferrite material N87				Compensation inductors' core PM/62/49, ferrite material N87			
	Capacitor unit: KEMET R76TF13305050J 3.3 nF (ESR=0.22 Ω)				Capacitor unit: EPCOS B32671L 6.8 nF (ESR=0.1 Ω)			

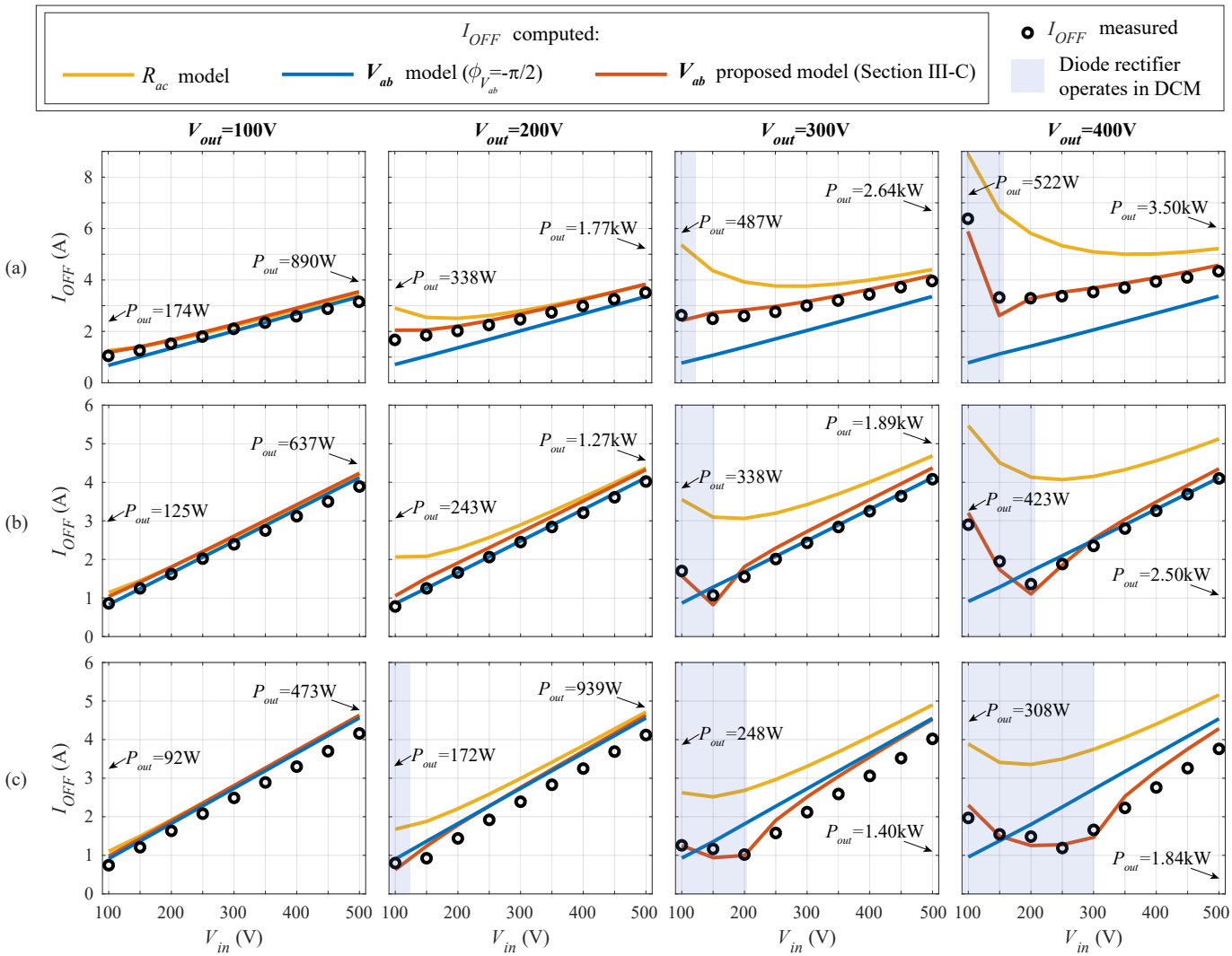

Fig. 6. Comparison between the measured and computed the inverter turn-off current I_{OFF} from the 3.7 kW IPT system in Fig. 5(a). The measurements are performed at: (a) M=M_{max}, (b) M=M_{mid}, (c) M=M_{min}. The shaded areas indicate the operating points in which the diode rectifier operates in DCM.

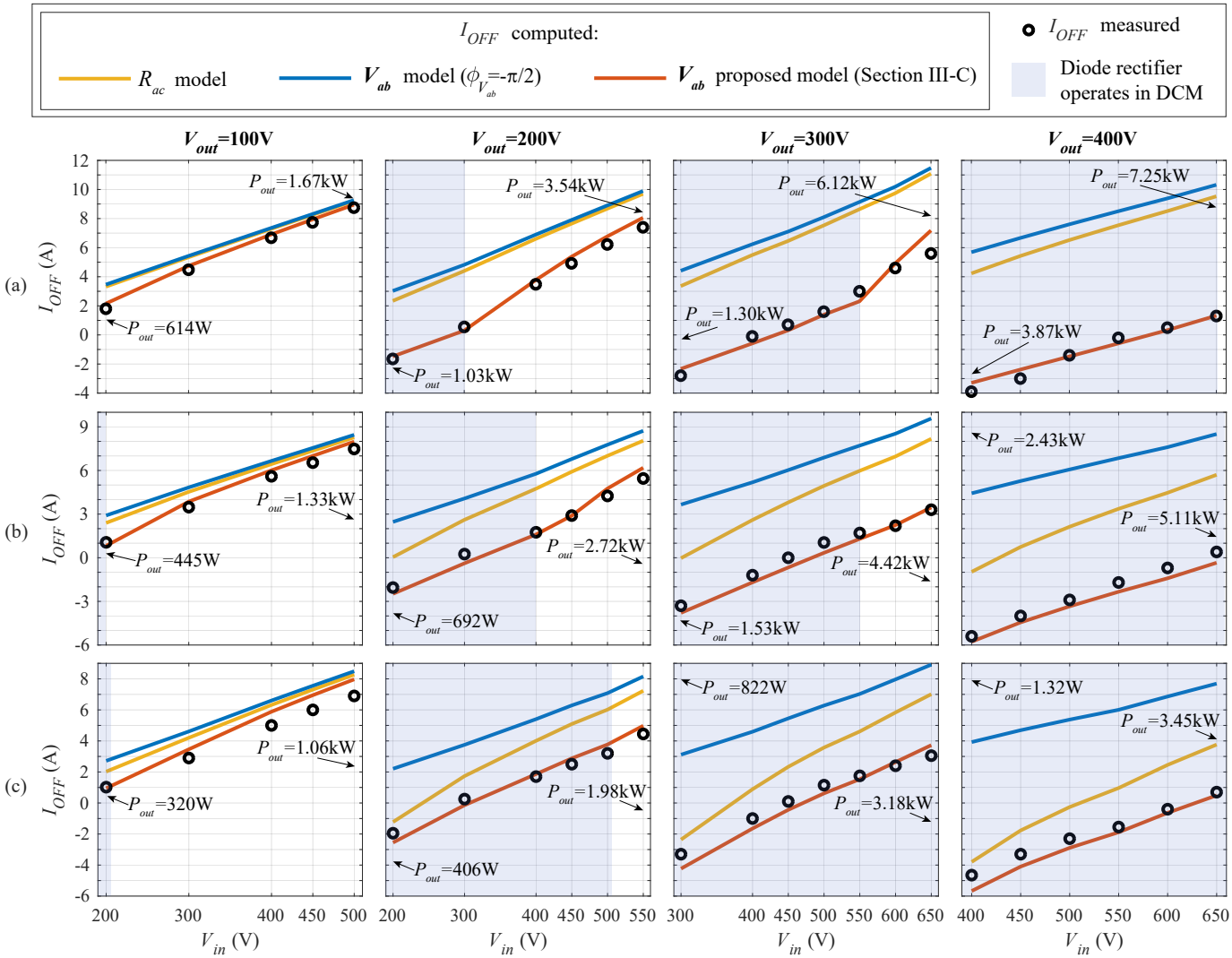

Fig. 7. Comparison between the measured and computed the inverter turn-off current I_{OFF} from the 7.7 kW IPT system in Fig. 5(b). The measurements are performed at: (a) M=M_{max}, (b) M=M_{mid}, (c) M=M_{min}. The shaded areas indicate the operating points in which the diode rectifier operates in DCM.

IPT system are the same of [16]. On the other hand, the coupled coils of the 7.7 kW IPT system follow reference designs of SAE J2954. For instance, the transmitting coil has been manufactured by MAGMENT while the receiving coil has been manufactured by PREMO. In both IPT systems, Delta Elektronika bidirectional power supplies SM1500-CP-30 are used as input and output voltage sources, corresponding to V_{in} and V_{out} illustrated in Fig. 1.

B. Measurements

In both IPT systems, the inverter turn-off current I_{OFF} has been measured at several operating points by sweeping both the DC input and output voltages. The inverter switching frequency has been set to 85 kHz in all cases. Moreover, three values of mutual inductance have been considered, as specified in Table II. In all these operating conditions, the measured I_{OFF} has been compared with the computed values from three different analytical models, which, respectively, consider the load as:

- the equivalent resistance R_{ac} in Fig. 2(a);
- the voltage source $\boldsymbol{V_{ab}}$ in Fig. 2(b), with $\phi(V_{ab})$=$-\pi/2$;
- the voltage source $\boldsymbol{V_{ab}}$ in Fig. 2(b), which $\phi(V_{ab})$ has been computed according to the proposed method in Section III-B.

The comparison of the measured I_{OFF} values and those computed from the analytical models is shown in Fig. 6 for the 3.7 kW IPT system and in Fig. 7 for the 7.7 kW IPT system.

C. Discussion

According to Fig. 6 and Fig. 7, the proposed estimation method can predict I_{OFF} more accurately than the other methods using a conventional load modeling strategy in both IPT systems. It is worth mentioning that this analysis has been performed for a wide range of operating conditions, i.e., with broad input and output voltage variations, and for three values of coils' alignments. The proposed method can also effectively estimate I_{OFF} when the diode rectifier operates in DCM, whereas other conventional methods would lead to significant errors. These results confirm that it is necessary to model the diode rectifier's conduction to estimate I_{OFF} accurately.

The precision achieved in estimating I_{OFF} is reasonable, and errors may be due to assumptions made in the proposed model and to variations in circuit parameters that occur during operation. The proposed model could be further improved if the dead time of v_{AB} were considered, which would undoubtedly add complexity. Currently, the accuracy of the proposed model, which excludes dead time, is deemed satisfactory.

V. Conclusion

A computation method for the inverter current distortion has been proposed for IPT systems utilizing the double-sided DLCC compensation. This is the analytical basis for assessing whether the inverter operates in ZVS turn-on. The proposed model has proven to be effective for a wide range of operating conditions, considering two distinct IPT systems. It has been demonstrated that the modeling of the diode rectifier's conduction is fundamental to achieving an accurate estimation of the inverter's turn-off current. For instance, the proposed model for the equivalent load shows considerable improvements compared to the conventional ones, which employ either an equivalent resistance or a voltage source with a fixed phase angle as the load.

Future research could investigate the effect of the inverter's dead time on the proposed model to further enhance its accuracy. Additionally, this method could be adapted for other IPT systems that present a distorted inverter's current.

References

[1] *J2954: Wireless Power Transfer for Light-Duty Plug-In/ Electric Vehicles and Alignment Methodology*, SAE International Std., August 2022.

[2] W. Zhang and C. C. Mi, "Compensation topologies of high-power wireless power transfer systems," *IEEE Transactions on Vehicular Technology*, vol. 65, pp. 4768 – 4778, 2016.

[3] H. Feng, T. Cai, S. Duan, J. Zhao, X. Zhang, and C. Chen, "An lcc-compensated resonant converter optimized for robust reaction to large coupling variation in dynamic wireless power transfer," *IEEE Transactions on Industrial Electronics*, vol. 63, no. 10, pp. 6591–6601, 2016.

[4] W. Li, H. Zhao, J. Deng, S. Li, and C. C. Mi, "Comparison study on ss and double-sided lcc compensation topologies for ev/phev wireless chargers," *IEEE Transactions on Vehicular Technology*, vol. 65, no. 6, pp. 4429–4439, 2016.

[5] S. Li, W. Li, J. Deng, T. D. Nguyen, and C. C. Mi, "A double-sided lcc compensation network and its tuning method for wireless power transfer," *IEEE Transactions on Vehicular Technology*, vol. 64, no. 6, pp. 2261–2273, 2015.

[6] W. Li, H. Zhao, S. Li, J. Deng, T. Kan, and C. C. Mi, "Integrated LCC compensation topology for wireless charger in electric and plug-in electric vehicles," *IEEE Transactions on Industrial Electronics*, vol. 62, no. 7, pp. 4215–4225, 2015.

[7] T. Kan, T.-D. Nguyen, J. C. White, R. K. Malhan, and C. C. Mi, "A new integration method for an electric vehicle wireless charging system using lcc compensation topology: Analysis and design," *IEEE Transactions on Power Electronics*, vol. 32, no. 2, pp. 1638–1650, 2017.

[8] Y. Chen, H. Zhang, C.-S. Shin, C.-H. Jo, S.-J. Park, and D.-H. Kim, "An efficiency optimization-based asymmetric tuning method of double-sided *LCC* compensated wpt system for electric vehicles," *IEEE Transactions on Power Electronics*, vol. 35, no. 11, pp. 11 475–11 487, 2020.

[9] W. Li, Q. Zhang, H. Li, C. Cui, and G. Wei, "Series filter computation method for ccm recovery in double side lcc wpt system," *IEEE Transactions on Industrial Electronics*, pp. 1–1, 2021.

[10] R. L. Steigerwald, "A comparison of half-bridge resonant converter topologies," *IEEE Trans. Power Electron.*, vol. 3, no. 2, pp. 174–182, 1988.

[11] C.-S. Wang, G. Covic, and O. Stielau, "General stability criterions for zero phase angle controlled loosely coupled inductive power transfer systems," in *IECON'01. 27th Annual Conference of the IEEE Industrial Electronics Society (Cat. No.37243)*, vol. 2, 2001, pp. 1049–1054 vol.2.

[12] Y. Guo, L. Wang, Y. Zhang, S. Li, and C. Liao, "Rectifier load analysis for electric vehicle wireless charging system," *IEEE Transactions on Industrial Electronics*, vol. 65, no. 9, pp. 6970–6982, 2018.

[13] Y. Guo, Y. Zhang, W. Zhang, and L. Wang, "Battery parameter identification based on wireless power transfer system with rectifier load," *IEEE Transactions on Industrial Electronics*, vol. 68, no. 8, pp. 6893–6904, 2021.

[14] F. Grazian, P. van Duijsen, T. B. Soeiro, and P. Bauer, "Advantages and tuning of zero voltage switching in a wireless power transfer system," in *IEEE PELS Workshop on Emerging Technologies: Wireless Power (WoW)*, 2019.

[15] *J2954 (R) Wireless Power Transfer for Light-Duty Plug-In/ Electric Vehicles and Alignment Methodology*, SAE International Std., Aug. 2022.

[16] F. Grazian, T. B. Soeiro, and P. Bauer, "Inductive power transfer based on variable compensation capacitance to achieve an ev charging profile with constant optimum load," *IEEE Journal of Emerging and Selected Topics in Power Electronics*, pp. 1–1, 2022.